Chinese Journal of Chemical Engineering 94 (2026) 280–290

Contents lists available at ScienceDirect

Chinese Journal of Chemical Engineering

journal homepage: www.elsevier.com/locate/CJChE

Full Length Article

Temperature-dependent fluidization behavior of silica sand in a deep bubbling fluidized bed

Ali Can Sivri [1,*], Amoolya Lalsare [2], Xi Gao [3,4]

[1] Department of Mechanical and Aerospace Engineering, West Virginia University, Morgantown, WV 26506, USA
[2] Department of Chemical and Biomedical Engineering, West Virginia University, Morgantown, WV 26506, USA
[3] Department of Chemical Engineering, Guangdong Technion-Israel Institute of Technology, Shantou 515063, China
[4] Wolfson Department of Chemical Engineering, Technion-Israel Institute of Technology, Haifa 3200003, Israel

ARTICLE INFO

Article history:
Received 20 July 2025
Received in revised form
3 November 2025
Accepted 4 November 2025
Available online 9 February 2026

Keywords:
Bubbling fluidized bed
Temperature effect
Pressure drop
Minimum fluidization velocity
Silica sand

ABSTRACT

This study investigates the impact of temperature on the fluidization behavior of a bench-scale deep fluidized bed using Group B silica sand particles as the material. Covering a temperature range of 200 °C to 800 °C, the experiments employed a transparent cold flow rig for visualizing bed behavior and a bench-scale bubbling fluidized bed reactor for pressure drop measurements at elevated temperatures. Pressure differentials over the distributor plate and bed were measured at two different bed aspect ratios (3.33 and 4.83). Results show that increasing temperature from ambient to 800 °C led to a significant reduction in the minimum fluidization velocity (U_{mf}), by 27% for 200 g and 35% for 300 g bed materials. Bed aspect ratio had negligible effects on U_{mf} but notably influenced bed pressure drop. Experimentally determined Archimedes (Ar) and Reynolds (Re) numbers differed from empirical correlations, highlighting the need for further investigation into temperature effects on fluidization hydrodynamics. A new correlation for U_{mf} prediction, based on experimental data, exhibited a low average error of 7.4%. These findings, along with detailed material characteristics, offer insights for future research on temperature effects in narrow-deep bubbling fluidized beds, particularly at low Re. The experimental data serve as a benchmark for verifying, validating, and optimizing numerical models and scaling studies.
© 2026 The Chemical Industry and Engineering Society of China, and Chemical Industry Press Co., Ltd. All rights are reserved, including those for text and data mining, AI training, and similar technologies.

1. Introduction

The expanded utilization of syngas, alternatively referred to as producer gas and primarily composed of hydrogen-rich synthetic gas, has the potential to reduce both greenhouse gas emissions and particulate matter emissions from power generation and transportation [1,2]. Furthermore, syngas finds applications in various chemical production processes. Syngas can be obtained through thermo-chemical conversion processes such as gasification, involving diverse feedstocks like biomass [3–5], coal [6], or municipal waste.

Fluidized-bed reactors are widely used because of their superior mixing and high heat transfer capabilities compared to other reactor types [7,8]. Among these, the bubbling fluidized bed gasifier (BFBG) stands out as a particularly versatile configuration, where the bed and feedstock particles are suspended and mixed by an upward flow of fluidizing gas [9]. Aside from its cost-effective operation and maintenance, BFBG also demonstrates versatility in accommodating a broad spectrum of feedstock types and particle sizes [10,11].

In order to achieve an effective gasification process within a BFBG, it's essential to adjust operational parameters to achieve the optimal fluidization quality. Therefore, understanding the hydrodynamics of fluidization is critical for enhancing the efficiency of gasification operations in BFBGs. A significant number of variables affect the fluidization hydrodynamics in addition to the fluidizing gas velocity (U_g). One of the critical parameters involves the bed aspect ratio, defined as the ratio of the bed height (H_p) to the bed diameter (D_b). This parameter impacts temperature gradients, residence time of the fluidizing fluid, particle mixing, and chemical reaction time. Particle size, sphericity, and density of both the bed and feedstock materials also play pivotal roles. For instance,

* Corresponding author.
E-mail address: acsengresearch@gmail.com (A.C. Sivri).

https://doi.org/10.1016/j.cjche.2025.11.029
1004-9541/© 2026 The Chemical Industry and Engineering Society of China, and Chemical Industry Press Co., Ltd. All rights are reserved, including those for text and data mining, AI training, and similar technologies.

Geldart [12] identified that particles falling within Group B of their classification, characterized by a size distribution of 150 to 500 μm and densities ranging from 1400 to 4000 $kg \cdot m^{-3}$, exhibit favorable fluidization behavior. Moreover, process temperature affects the fluid viscosity and temperature [13], the inter-particle attraction force [14], heat transfer rates [13,15], *etc*., therefore it affects both the fluidization hydrodynamics and chemistry.

However, equations and correlations governing fluidization behavior are primarily derived from measurements conducted at ambient conditions, often referred to as "cold flow" studies. These conditions significantly differ from the high-temperature flow and chemical processes occurring inside a BFBG, particularly under actual operational conditions and at the microscales relevant for process optimization and scaling. Moreover, temperature fluctuations inherent to the gasification process must be considered in calculations due to their non-negligible impact [16]. The presence of conflicting assertions within academic literature regarding the influence of temperature on fluidization hydrodynamics highlights the complexity surrounding this phenomenon. For instance, Lin *et al.* [17] investigated agglomeration behavior in a straw-fired laboratory-scale fluidized bed combustor and found that elevated temperatures reduce defluidization time due to the formation of potassium-rich molten ash coatings on sand particles. This increased stickiness accelerates agglomeration and raises the minimum fluidization velocity (U_{mf}) above theoretical predictions at high temperatures. The study clearly demonstrated that the onset of sintering effects plays a critical role in modifying fluidization behavior. Similarly focusing on temperature effects, Pattipati and Wen [18] measured the U_{mf} of sand particles in a 13.2 cm diameter hot fluidized bed with a bed aspect ratio of less than 1, and found that U_{mf} decreases with increasing temperature for small particles (<2 mm) due to reduced gas density and viscosity. In contrast, U_{mf} increases with temperature for larger particles (>2 mm). They also confirmed that Wen and Yu's correlation remains valid at elevated temperatures, although the experimental data showed no consistent monotonic trend across all particle sizes. These studies were supported and extended by Botterill *et al.* [19], who conducted high-temperature fluidization experiments in a 188 mm diameter bed, using a wide range of sand particle sizes from Geldart Groups B and D. While the exact static bed height was not reported, pressure transducer taps were spaced 14–23 mm apart vertically, implying a fluidized region of appreciable height. The authors found that U_{mf} decreases with increasing temperature for smaller Group B particles due to reduced gas viscosity and density. In contrast, larger Group D particles showed an initial increase in U_{mf} with temperature due to dominant turbulent flow and gas density effects. At even higher temperatures, U_{mf} began to decrease again as the flow transitioned to laminar. The study highlighted the critical influence of temperature-dependent voidage and Reynolds (*Re*) number regimes, and emphasized that most standard U_{mf} correlations are inaccurate unless corrected for temperature effects. Similarly, Al-Farraji and Taofeeq [20] experimentally investigated the effect of temperature and particle size on U_{mf} in an atmospheric bubbling fluidized bed with bed aspect ratios of 0.5 and 1, using silica sand in the 300–710 μm range and operating up to 850 °C. They observed that U_{mf} decreased with temperature up to about 700 °C, beyond which it plateaued. They also found that particle size had a direct positive effect on U_{mf}, while bed height had no measurable impact. Common empirical correlations failed to predict U_{mf} accurately at high temperatures, leading them to propose a new correlation with a mean relative deviation below 5.5%.

Across all these studies, a recurring issue is the poor predictive performance of classical U_{mf} correlations, particularly at elevated temperatures. Anantharaman *et al.* [21] analyzed this issue and conducted a comprehensive review of more than 100 U_{mf} correlations and concluded that large discrepancies in predictions—up to six orders of magnitude—are common, especially for Geldart Group A and B particles. The study emphasized that most correlations are based on limited empirical datasets and often include parameters such as voidage and sphericity that introduce nonphysical trends. The authors concluded that a universal mechanistic correlation is currently intractable and called for the development of better-informed and data-driven models, particularly under non-ambient conditions. Yates [22] presented a literature synthesis showing that temperature effects are highly system-specific, with both increasing and decreasing trends reported.

These discrepancies highlight the complex relationship between thermal, geometric, and material factors influencing fluidization. However, several aspects remain insufficiently addressed in the literature, particularly the combined effect of temperature and bed aspect ratio in deep narrow beds, and the validity of traditional empirical U_{mf} correlations under high-temperature, low-*Re* conditions. The present study aims to fill these gaps by providing experimental insight into the temperature-dependent fluidization behavior of Group B silica sand in a deep bubbling fluidized bed up to 805 °C.

The main aim of this research is to examine how temperature affects fluidization hydrodynamics in a bench-scale (narrow) deep bed and to compare these observations with some of the established correlations in the literature. Additionally, this research endeavors to contribute valuable empirical data to the existing body of literature in the field. To accomplish this objective, two different experimental setups were utilized. The first involved a cold-flow rig designed with geometry and dimensions identical to those of the bench-scale BFBG. This setup aimed to examine the correlations between parameters such as the pressure drop across the distribution plate, pressure drop across the bed, minimum fluidization velocity, and bed aspect ratio, among others [23]. The second experimental setup, the bench-scale BFBG, was designed for high-temperature operation (approximately 800 °C) to assess the temperature effect on the aforementioned correlations when using biomass, coal, or biomass-coal mixtures as feedstock materials.

2. Methods

2.1. Minimum fluidization velocity

As noted earlier, the U_{mf} holds significant importance in determining the minimum fluidization state and regulating the fluidization characteristics within the BFBG. Numerous correlations that forecast U_{mf} are based on factors such as the average particle size and sphericity of the binary mixture material. The Ergun equation [24], for instance, establishes a correlation between the pressure drop across a packed bed of non-spherical particles and various characteristics of the fluidizing gas and bed particles:

$$\frac{\Delta P_{bed}}{H} = \frac{150(1-\varepsilon)^2}{\varepsilon^3}\frac{\mu_f U_g}{(\phi d_p)^2} + \frac{1.75(1-\varepsilon)}{\varepsilon^3}\frac{\rho_f U_g^2}{\phi d_p} \quad (1)$$

The pressure drop along the bed height (ΔP_{bed}) is determined by several parameters, including H (bed height), ε (bed voidage), μ_f (fluidizing gas viscosity), d_p (mean bed particle diameter), ρ_f (gas density), and ϕ (average bed particle sphericity). Bed voidage (ε) represents the proportion of the total volume occupied by voids between bed particles relative to the overall bulk bed volume:

$$\varepsilon = 1 - \frac{\rho_b}{\rho_s} \tag{2}$$

here, ρ_b represents the bulk density, calculated as the ratio of the mass (m_b) to the volume (V_b) of the bulk material. Additionally, ρ_s denotes the bed skeletal density, defined as the density of the bed material excluding any porosity.

When the superficial gas velocity (U_g) equals the U_{mf}, the pressure drop across the bed (ΔP_{bed}) equals the pressure drop at minimum fluidization (ΔP_{mf}), where the subscript "mf" denotes values at the minimum fluidization condition. A control volume analysis assumes that the mass of the bed material (W) is equal to the product of the ΔP_{bed} and the cross-sectional area of the bed at minimum fluidization. Additionally, it is assumed that fluidization of the bed occurs due to the summation of drag forces acting on individual bed particles, with the total drag force (D) equating to the W:

$$D = \Delta P_{mf} A = W \tag{3}$$

$$W = mg = AH_{mf}\left(1 - \varepsilon_{mf}\right)\left(\rho_p - \rho_g\right)g \tag{4}$$

$$D = \sum D_{p,i} = \sum \frac{1}{2} C_{D,i} \rho_g U_{g,i}^2 A_{p,i} \tag{5}$$

here, D represents the total drag force acting on the bed particles; ΔP_{mf} denotes the pressure drop across the bed; A signifies the cross-sectional area of the bed; m represents the mass of the bed material; g denotes the acceleration due to gravity; H_{mf} represents the height of the bed and ε_{mf} signifies the bed voidage under minimum fluidization conditions; ρ_p represents the particle density; ρ_g signifies the density of the fluidizing gas; $D_{p,i}$ represents the drag force exerted on particle i; $C_{D,i}$ denotes the drag coefficient for particle i; $U_{g,i}$ represents the local velocity of the fluidizing gas; and $A_{p,i}$ signifies the characteristic area of particle i.

To determine U_{mf} practically, bed pressure and flow rate measurements are commonly used, employing graphical methods. This involves plotting ΔP_{bed} against U_g, as shown in Fig. 1, where U_{mf} is identified at the intersection of the slope of bed pressure under fixed-bed conditions and the constant bed pressure drop for full fluidization. Initial fluidization velocity (U_{if}) and complete fluidization velocity (U_{cf}) mark the points of fluidization initiation and full development, respectively. U_{if} represents the minimum gas velocity, which starts deviating from the linear trend of the fixed-bed state. U_{cf} represents the minimum required gas velocity where the transition from fixed-bed state to complete fluidization is completed, and the pressure drop value is almost constant. U_{if} and U_{cf} can be determined graphically using the intersection point of the pressure drop value with the gas velocity at the ΔP_{bed} *versus* U_g graph, as shown in Fig. 1. The initial state of the bed (voidage and packing pattern) has been taken into account.

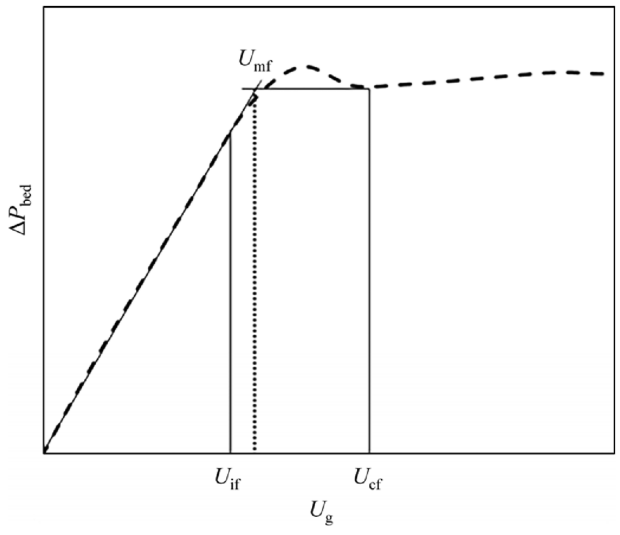


Fig. 1. Illustration of the graphical method for determining U_{mf}, U_{if}, and U_{cf}.

Moreover, Eq. (1) can be reformulated to align with the minimum fluidization condition:

$$\frac{\rho_f\left(\rho_p - \rho_f\right)g d_p^3}{\mu_f^2} = \frac{150\left(1 - \varepsilon_{mf}\right)}{\phi^2 \varepsilon_{mf}^3}\left(\frac{\rho_f U_{mf} d_p}{\mu_f}\right) + \frac{1.75}{\phi \varepsilon_{mf}^3}\left(\frac{\rho_f U_{mf} d_p}{\mu_f}\right)^2 \tag{6}$$

Furthermore, various investigations have established correlations between U_{mf} and dimensionless Archimedes (Ar) and Reynolds (Re) numbers. The choice of Ar and Re is motivated by their ability to represent the competing forces governing fluidization. Ar reflects the ratio of buoyancy and gravitational forces to viscous forces, while Re expresses the ratio of inertial to viscous forces. Both quantities depend on gas density and viscosity, which vary with temperature. As temperature increases, gas density decreases while viscosity increases, leading to lower Ar and Re values and reducing U_{mf}. Therefore, using Ar and Re provides a physically meaningful framework for generalizing fluidization correlations under different thermal conditions. The definitions of Ar and Re are as follows:

$$Ar = \frac{\rho_f\left(\rho_p - \rho_f\right)\left(g d_p^3\right)}{\mu_f^2} \tag{7}$$

$$Re_{mf} = \frac{\rho_f U_{mf} d_p}{\mu_f} \tag{8}$$

These relationships allow Eq. (1) to be expressed as a function of Ar and Re:

$$Ar = \frac{150\left(1 - \varepsilon_{mf}\right)}{\phi^2 \varepsilon_{mf}^3} Re_{mf} + \frac{1.75}{\phi \varepsilon_{mf}^3} Re_{mf}^2 \tag{9}$$

Many empirical correlations have been formulated utilizing Eq. (8) to forecast the U_{mf}. Table 1 presents selected correlations from the literature that relate Ar and Re for silica sand Geldart Group B particles, allowing for comparison with the results obtained in this study.

2.2. Cold and hot fluidization experiments setups

As previously outlined in the Introduction, this study employed two distinct experimental setups to comprehensively investigate fluidization hydrodynamics. This section provides detailed descriptions of these setups and the methodologies employed.

Fig. 2 and Table 2 provide a detailed overview of the cold flow test rig and its specifications. Most components are made of acrylic for visual monitoring of various phenomena like bed heights, bubble formation, and particle behavior. Air served as the fluidizing medium, with the flow rate controlled by a mass flow controller. The distributor plate, made of 316L stainless steel, featured a 10-μm pore size and 39% total porosity.

Nine vertically aligned pressure tabs, positioned from just below the distributor plate to just below the transition cone, monitored pressures within the rig during experiments. Pressure

Table 1
Selected correlations for determining U_{mf} for silica sand.

Abbreviation	Correlation	Author(s)
A1	$Re = \left(25.46^2 + 0.0382Ar\right)^{0.5} - 25.46$	Bourgeois and Grenier [25]
A2	$Re = (0.000822Ar)^{0.94}$	Leva [26]
A3	$Re = \left(30.28^2 + 0.0464Ar\right)^{0.5} - 30.28$	Paudel and Feng [27]
A4	$Re = Ar/1502$	Subramani *et al.* [28]
A5	$Re = \left(31.6^2 + 0.0425Ar\right)^{0.5} - 31.6$	Thonglimp *et al.* [29]
A6	$Re = \left(33.7^2 + 0.0408Ar\right)^{0.5} - 33.7$	Wen and Yu [30]
A7	$Re = \left(30.85^2 + 0.0379Ar\right)^{0.5} - 30.85$	Wu and Baeyens [31]
A8	$Re = \left(18.75^2 + 0.03125Ar\right)^{0.5} - 18.75$	Zhu *et al.* [32]

taps 1 and 2 measured pressure drop across the distributor plate, while taps 2 to 8, spaced at intervals of 38 mm, allowed pressure measurements at different heights within the bed. A pressure transmitter and seven additional pressure transducers were employed for data collection, with a sampling rate of 10 Hz, interfaced with the data acquisition system. High-speed images of the bed behavior were captured using a Photron FASTCAM SA5 camera (Japan). Images were recorded at a resolution of 1024 × 1024 pixels and a sampling frequency of 100 frames per second. Each image was then cropped to extract only the column region, resulting in column images of 128 × 1024 pixels.

Representative snapshots (see Fig. 6) were selected based on the clarity and representativeness of the observed bed behavior. Because bubble formation was not always equally visible at all gas velocities, the chosen frames correspond to conditions where bubble formation was most clearly observed through the acrylic wall of the cold flow rig. In some cases, it was not fully visible. For bed expansion, snapshots were taken when the bed height reached a quasi-maximum value, representing near-maximum expansion but not necessarily the absolute maximum. The fluidizing gas flow rate was gradually increased in 1 standard $L \cdot min^{-1}$ increments (equivalent to approximately 0.0146 $m \cdot s^{-1}$ in superficial velocity), and high-speed images were recorded at each step above the minimum fluidization condition. Each test was repeated three times, with recordings of at least 30 s, and statistical analysis confirmed that no significant differences existed between repetitions, ensuring reproducibility of the results.

Table 2
Cold flow rig dimensions.

Parameter	Value
Diameter/mm	38
Height/mm	406
Transition cone height/mm	25
Freeboard diameter/mm	76
Freeboard height/mm	254

Fig. 3 depicts the experimental setup for the bench-scale BFBG. The BFBG reactor is made of Inconel and has the same dimensions and sections as in the cold flow rig. The test rig utilizes a furnace that can reach temperatures up to 1500 °C. Temperature measurements in the bench-scale BFBG reactor were performed with K-type thermocouples (Omega™) positioned at the middle of the outer reactor wall and just above the bed material, connected to the same data acquisition system with a sampling frequency of 10 Hz. Pressure measurements were made using the same transducers and data acquisition system as in the cold flow rig test stand. Pressure tabs are positioned at the same intervals as in the cold flow rig along the bed height. Additionally, 0.5 μm filters are installed in the product gas and pressure transducer lines to prevent particle entrainment. Experimental conditions and sand properties are summarized in Table 3, with pressure measurements taken for at least 30 s at each flow rate after allowing for stabilization.

2.3. Material analysis and preparation

The bed material selected for this study was silica sand (commercial grade fine sand, Quikrete, USA), sieved in a range of 300 μm to 500 μm to achieve Geldart Group B requirements. After the sieving, dynamic image analysis (Model QICPIC, Sympatec GmbH, Germany) was used to measure silica sand particle size and shape distribution. Fig. 4(a) is typical of the images used for the analysis, which showed that 90% of the sand particles had a sphericity distribution between 0.85 and 0.95, and an average sphericity of 0.86. The analysis further revealed that 90% of the particles are within the size range of 309 μm to 461 μm, with an average size of 368 μm. Fig. 4(b) and (c) show the particle size

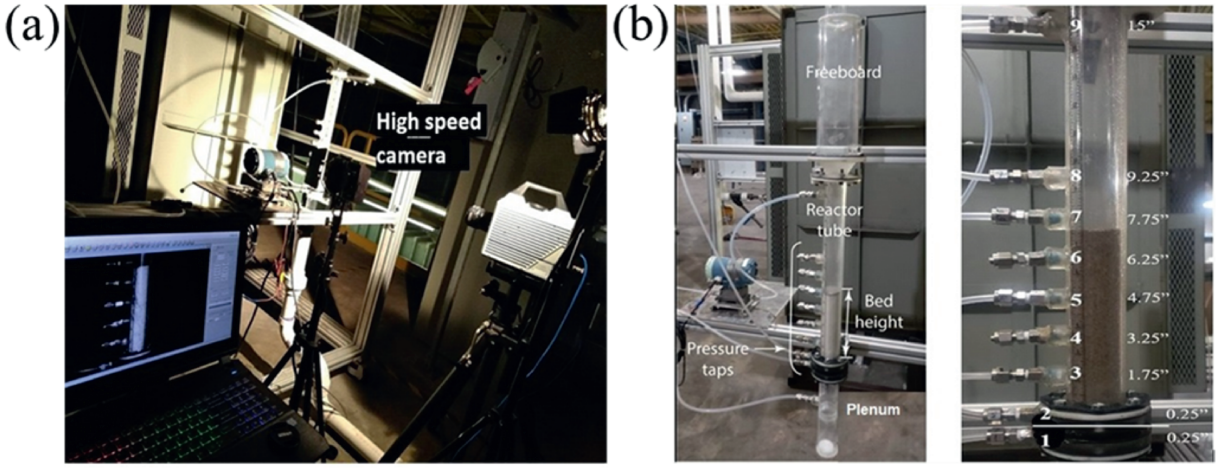


Fig. 2. Cold flow experimental setup: (a) high speed imaging, (b) cold-flow test rig of fluidized bed.

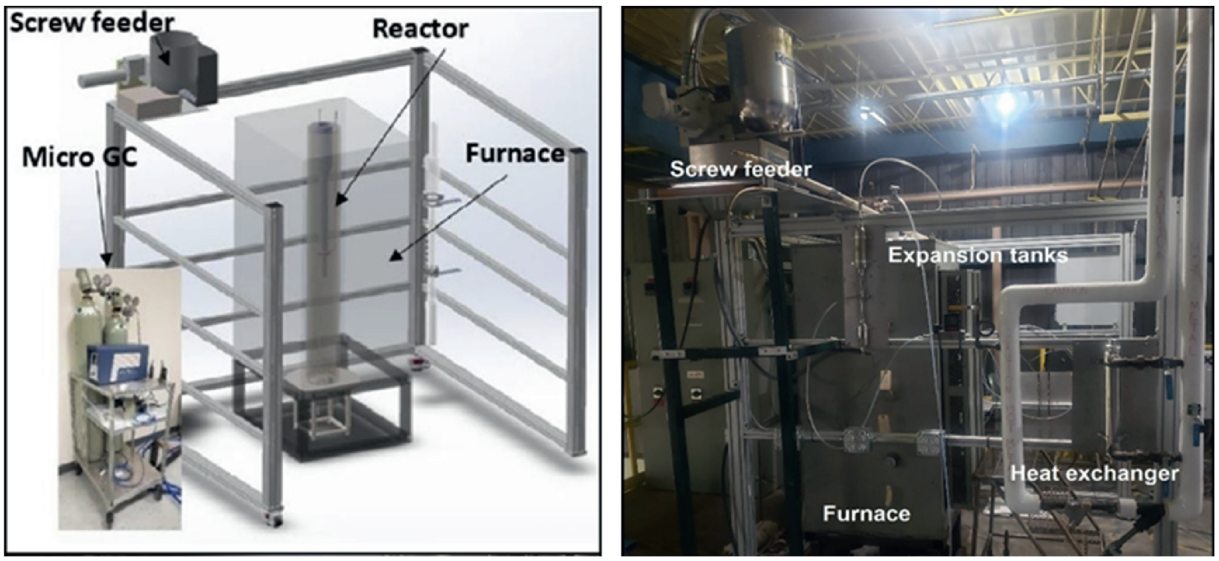


Fig. 3. BFBG experimental setup.

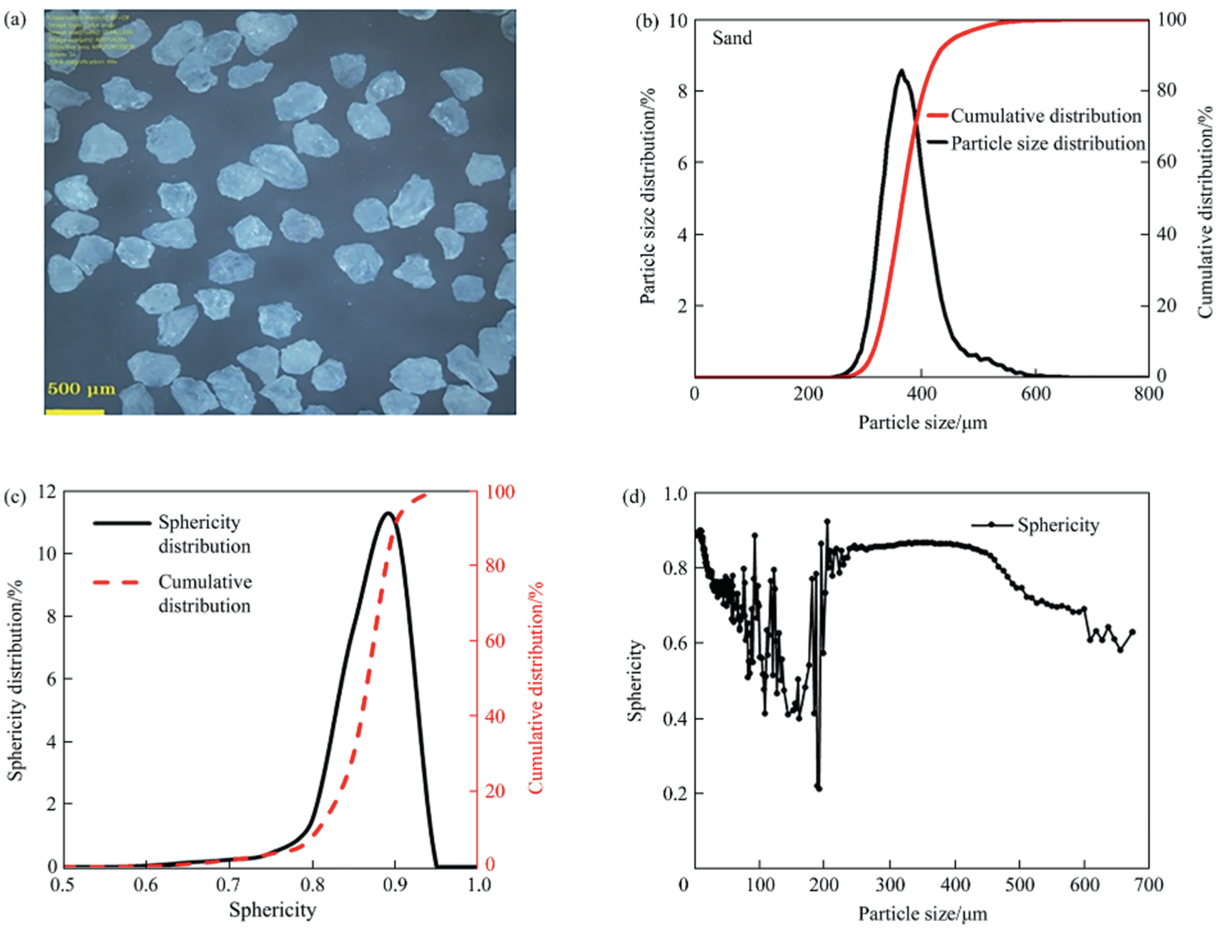


Fig. 4. (a) Image of silica sand Geldart Group B particles; (b) silica sand particles size distribution; (c) silica sand particles sphericity distribution; (d) sphericity change with particle size.

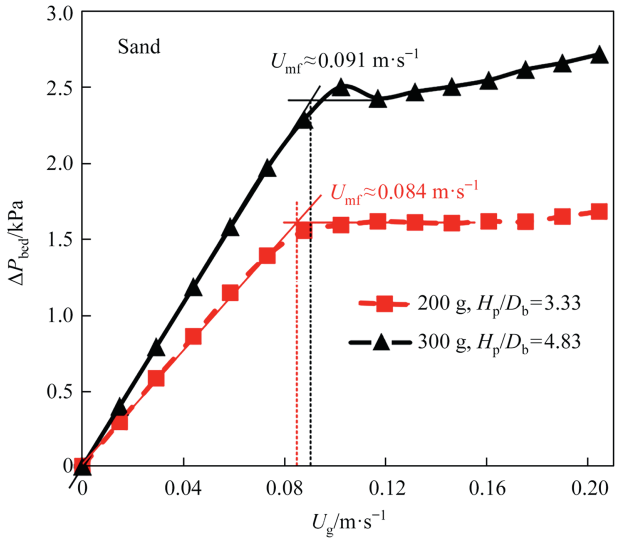


Fig. 5. Relationship between bed pressure drop and superficial air velocity at ambient temperature for silica sand masses of 200 g and 300 g, respectively.

distribution and sphericity, respectively. Fig. 4(d) presents how sphericity changes with the particle size. The details of sphericity and size distributions are provided in Table S1 of the Supplementary Material. Also, sand particle skeletal density was analyzed with a gas pycnometer.

3. Results and Discussion

This section showcases the experimental findings obtained under ambient conditions within the cold flow rig, and up to temperatures of 800 °C in the bench-scale BFBG. U_{mf} was determined using the graphical methodology. In addition, dimensionless *Ar* and *Re* numbers were calculated for each experimental condition, enabling a comprehensive comparison of the results with established correlations found in the literature.

3.1. Pressure drop and fluidization behaviors of cold flow

Fig. 5 illustrates the relationship between bed pressure drop and air velocity, with only sand used as the bed material in these experiments. The corresponding bed aspect ratio (static bed height/bed diameter) for 200 g and 300 g of sand were H_p/D_b = 3.33 and 4.83, respectively. These measurements indicate that the bed bulk density rose by approximately 3.5% when the sand mass increased by 50%, from 1380 to 1430 kg·m^{-3}, for 200 g and 300 g of sand, respectively. Additionally, at the minimum fluidization condition, the bed aspect ratios were measured as 3.66 and 5.33 for 200 g and 300 g, respectively. By employing Eq. (2), the bed voidage was determined to be 0.53 and 0.51 for the bed masses of 200 g and 300 g, respectively.

Table 3
Experimental conditions and sand properties.

Experimental condition	Hot flow	Cold flow
Temperature/°C	200–800	Ambient temperature
Fluidizing gas	Air	Air
Material mass/g	200, 300	200, 300
Gas velocity, U_g/m·s^{-1}	0–0.4	0–0.2
Sauter mean diameter/μm	368	
Average of sphericity	0.86	
Average bulk density of static bed/kg·m^{-3}	1430	
Voidage of static bed/%	46.02	
Skeletal density/kg·m^{-3}	2640	
Geldart Group	B	

Fig. 5 suggests that the transition to fluidization was smooth for the bed aspect ratio of 3.33, supported by the almost constant bed pressure drop after reaching this state. U_{mf} and ΔP_{bed} at the minimum fluidization for H_p/D_b = 3.33 were 0.084 m·s^{-1} and 1.54 kPa, respectively. The theoretical ΔP_{bed} at U_{mf} calculated with Eq. (2) was higher at 1.72 kPa, due to the narrow particle size distribution and high sphericity in the experiment.

Larger wall effects and increased bed bulk density associated with the increase in the bed aspect ratio affected the transition to fluidization, as seen in Fig. 5. Moreover, larger wall effects were the reason why the pressure drop kept increasing linearly with U_g, albeit with a smaller slope after entering the fluidization state. U_{mf} and the corresponding ΔP_{bed} for H_p/D_b = 4.83 were 0.091 m·s^{-1} and 2.37 kPa, respectively. Again, theoretical ΔP_{bed} at U_{mf} calculated with Eq. (2) was higher at 2.58 kPa compared to the measured value. In addition, the same *Ar* value of 3065 was obtained for both bed aspect ratios but different *Re* numbers (1.8 and 2, for 200 g and 300 g sand, respectively).

Fig. 6 illustrates the fluidization behavior of a mono-component bed consisting of silica sand with masses of 200 g

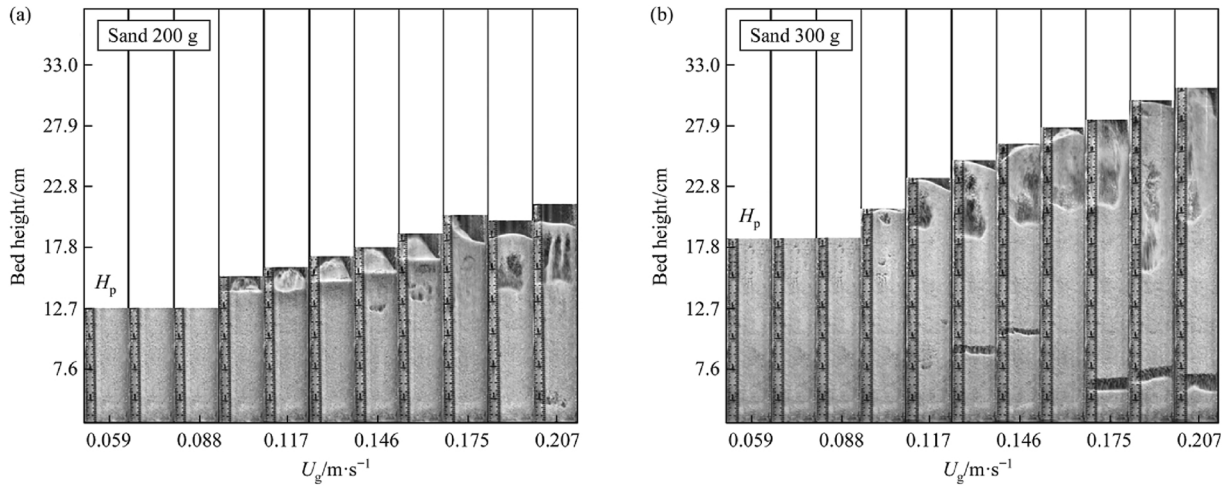


Fig. 6. Illustration depicting the fluidization behavior of (a) 200 g and (b) 300 g of the mono-component bed using silica sand.

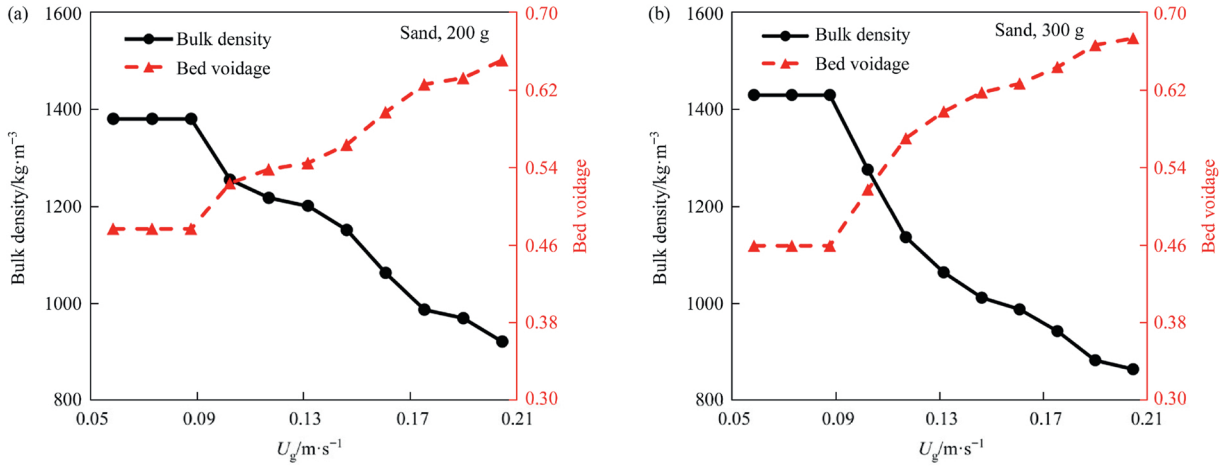


Fig. 7. Changes in bulk density and bed voidage with respect to superficial gas velocity for (a) 200 g and (b) 300 g of silica sand.

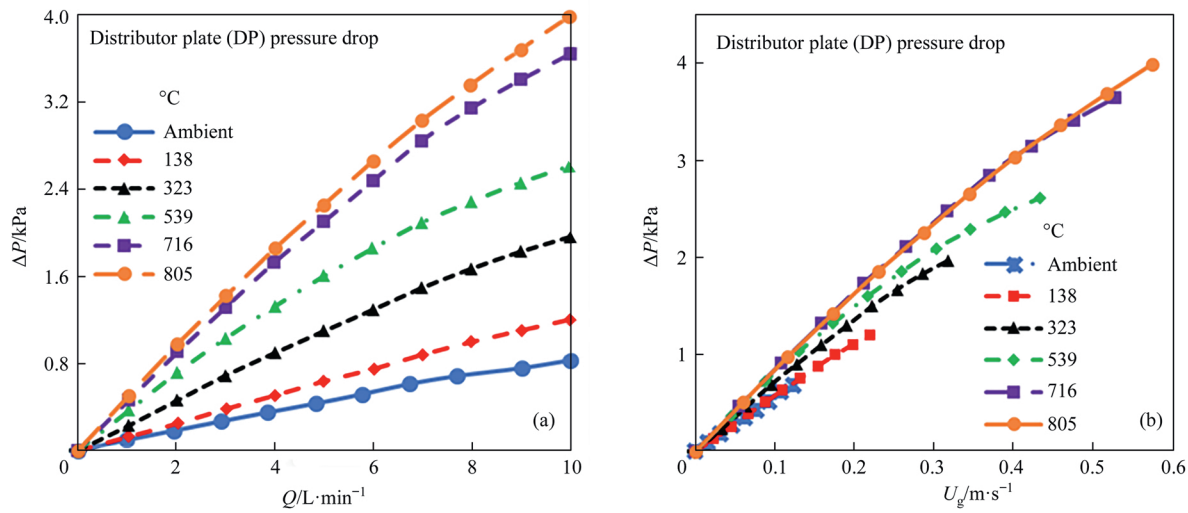


Fig. 8. The relationship between the pressure drop across the distributor plate and (a) air flow rate and (b) superficial gas velocity at various average temperatures.

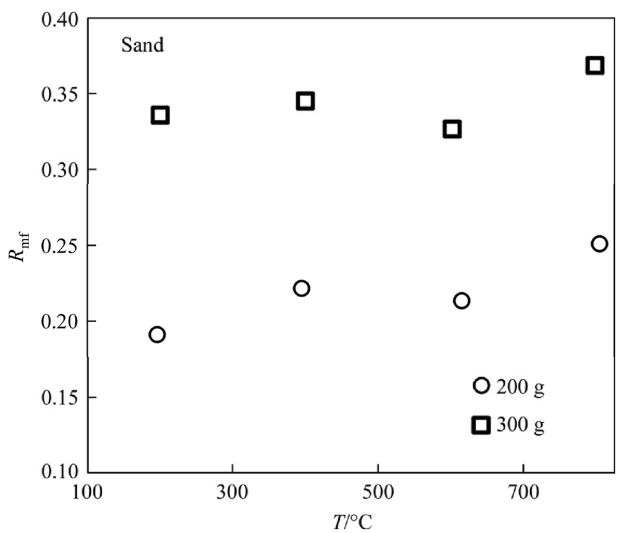


Fig. 9. Influence of temperature on the R_{mf}.

(Fig. 6(a), Case I, $H_p/D_b = 3.33$), and 300 g (Fig. 6(b), Case II, $H_p/D_b = 4.83$), depicting the variation with increasing fluidizing gas velocity. Minimum fluidization was achieved at a superficial gas velocity of 0.084 and 0.091 m·s^{-1} for Cases I and II, respectively, as shown in Fig. 5. Initial expansion of the bed occurred concurrently with the elutriation of small sand dust particles from the bed surface for both cases. For Cases I and II, initial bed expansion was observed during the transition from a superficial gas velocity of 0.088 to 0.103 m·s^{-1}, as seen in Fig. 6(a) and (b). In Case I, as the gas velocity increased further, smooth bubbling and bubbling regimes were observed until the gas velocity reached 0.146 m·s^{-1}. Later, by increasing the gas velocity more, slugs were being formed close to the bed surface. Superficial gas velocities higher than 0.175 m·s^{-1} caused flat slugs for Case I. For Case II, at the gas velocity of 0.117 m·s^{-1}, the bubbling regime was reached with the wall slugs close to the bed surface. Continued escalation in gas velocity led to the formation of slugs and bed segregation, resulting from potent interparticle forces and wall effects. In Case II, a high bed aspect ratio of 4.83 promoted the fast slug formation. Particle carryover was not observed even at the highest gas velocity of 0.207 m·s^{-1}.

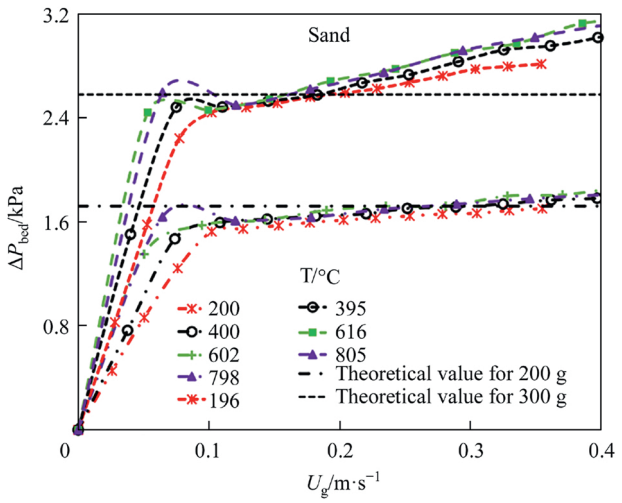


Fig. 10. The change in bed pressure drops with fluidizing gas velocity at different temperatures.

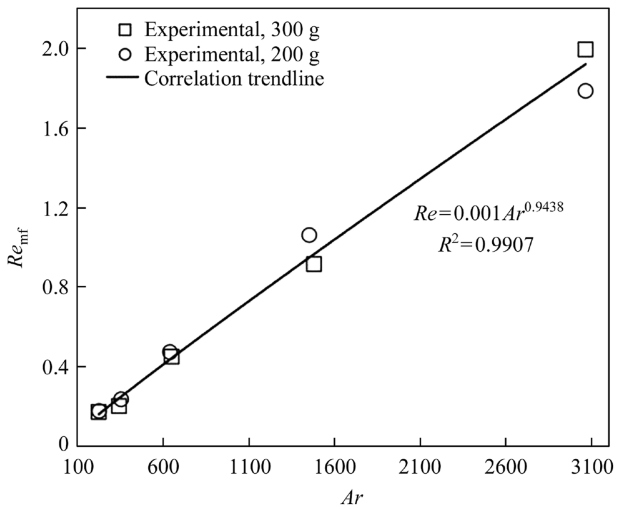


Fig. 11. Derivation of the new correlation, *Re versus Ar*.

Additionally, Fig. 7 illustrates the alterations in bulk density (ρ_b) and bed voidage (ε) for both Case I (sand, 200 g) and Case II (sand, 300 g). In both cases, bed voidage increases with the superficial gas velocity, and bulk density decreases accordingly. In Case II, ε increases rapidly and attains higher values than in Case I at the same superficial gas velocities, consistent with an earlier transition to the slugging regime in Case II. In Case I, after the onset of slugging, the decrease in ρ_b with increasing gas velocity becomes more apparent.

3.2. Impact of temperature on distributor plate pressure drop

In the Introduction, it is highlighted how the pressure drop across the bed and the uniformity of gas flow distribution above the porous disc surface are affected by the momentum flux of the flow leaving the distributor plate. This momentum flux is strongly influenced by the thermal expansion of the fluidizing gas. As temperature increases, viscosity rises and gas density decreases. Monitoring the pressure drop across the distributor plate is essential for understanding subsequent changes in bed pressure and fluidization quality.

Fig. 8 illustrates the pressure drop across the distributor plate, depicted as a function of temperature for various flow rates (Fig. 8(a)) and fluidizing gas velocities (Fig. 8(b)). Although the fluidizing gas flow rate had a linear influence on the distributor plate pressure drop, the temperature had a significant impact, especially at high flow rates.

In fluidized bed applications, achieving a uniform distribution of fluidizing gas above the distributor plate is paramount. The ratio of R_{mf}, defined as the pressure drop across the distributor plate to the pressure drop across the bed at minimum fluidization conditions, serves as a crucial parameter for maintaining consistent operation of the fluidized bed. In the case of bed masses of 200 g and 300 g, the R_{mf} values experienced a change from 0.19 to 0.25 and from 0.34 to 0.37, respectively, as the temperature rose from ambient to 800 °C (Fig. 9). These R_{mf} values fall within the ranges suggested by Zuiderweg [33] (Eq. (10)) and Siegel [34] (Eq. (11)) for ensuring stable and adequate operation.

Table 5
The comparison between the theoretical predictions of *Re* and the experimental Re_{exp}.

	200 g					300 g				
T/°C	798	602	400	200	25	805	616	395	196	25
Ar	225	355	639	1452	3065	224	343	650	1481	3065
Re_{exp}	0.18	0.24	0.47	1.06	1.79	0.17	0.20	0.45	0.92	1.99
A1	0.17	0.26	0.47	1.07	2.20	0.17	0.26	0.48	1.09	2.20
Error/%	4.7	12.3	0.5	0.6	23.4	2.7	26.6	7.4	18.8	10.6
A2	0.20	0.31	0.55	1.18	2.38	0.20	0.30	0.55	1.20	2.38
Error/%	15.9	33.1	15.5	11.3	33.5	18.4	50.4	23.3	31.4	19.6
A3	0.17	0.27	0.49	1.09	2.26	0.17	0.26	0.49	1.11	2.26
Error/%	2.6	14.7	2.7	3.0	26.8	0.6	29.3	9.8	21.7	13.6
A4	0.15	0.24	0.43	0.97	2.04	0.15	0.23	0.43	0.99	2.04
Error/%	15.1	0.1	10.0	8.9	14.3	13.4	12.9	3.8	7.7	2.4
A5	0.15	0.24	0.43	0.96	2.00	0.15	0.23	0.43	0.98	2.00
Error/%	14.5	0.8	9.7	9.3	11.9	12.7	13.6	3.5	7.1	0.2
A6	0.14	0.21	0.38	0.87	1.81	0.14	0.21	0.39	0.88	1.81
Error/%	23.0	9.2	18.6	18.2	1.2	21.4	2.3	13.0	3.4	9.4
A7	0.14	0.22	0.39	0.88	1.83	0.14	0.21	0.40	0.90	1.83
Error/%	21.9	7.9	17.5	17.1	2.4	20.2	3.8	11.8	2.1	8.3
A8	0.19	0.29	0.53	1.17	2.40	0.19	0.28	0.53	1.20	2.40
Error/%	5.7	24.4	11.1	10.6	34.4	7.9	40.2	18.7	30.6	9.0
A9	0.17	0.26	0.44	0.96	1.95	0.17	0.25	0.45	0.98	1.95
Error/%	6.0	8.1	6.0	9.1	9.3	4.0	22.1	0.4	7.3	2.1

Table 4
Summary of the temperature effect on the parameters (U_{mf}, ΔP_{mf}, Re_{mf}, and *Ar*) investigated.

200 g, $H_p/D_b = 3.33$					300 g, $H_p/D_b = 4.83$				
Temperature/°C	$\Delta P_{bed\text{-}mf}$/kPa	U_{mf}/m·s^{-1}	*Ar*	Re_{mf}	Temperature/°C	$\Delta P_{bed\text{-}mf}$/kPa	U_{mf}/m·s^{-1}	*Ar*	Re_{mf}
25	1.54	0.086	3065	1.80	25	2.37	0.096	3065	2.00
200	1.55	0.100	1452	1.06	196	2.48	0.085	1481	0.92
400	1.63	0.080	639	0.47	395	2.55	0.075	650	0.45
602	1.63	0.061	355	0.24	616	2.46	0.054	343	0.20
798	1.61	0.063	225	0.18	805	2.50	0.062	224	0.17

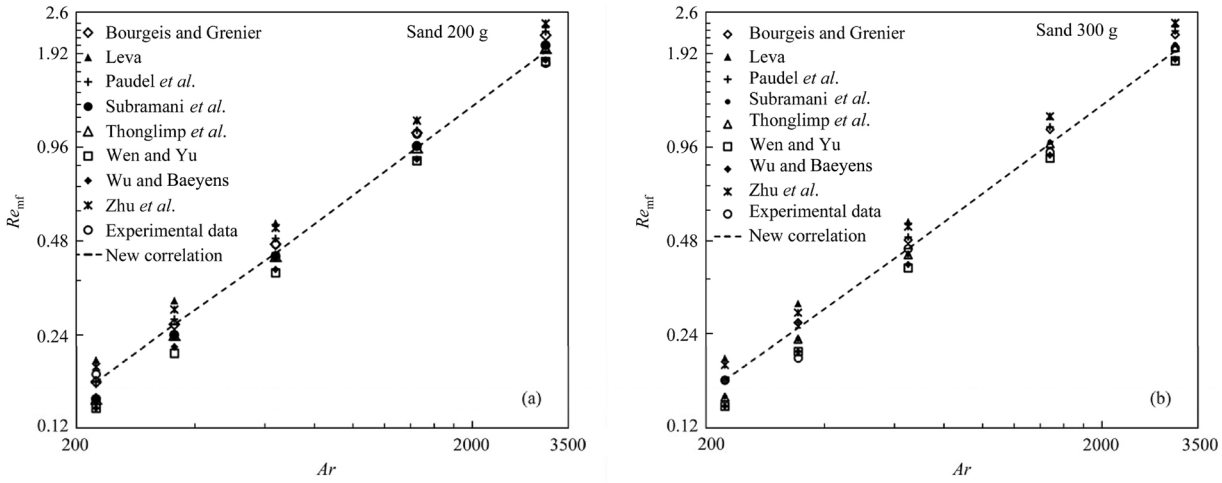


Fig. 12. The variation of the predicted and experimental Re_{mf} values with the increasing *Ar* for silica sand masses of (a) 200 g, and (b) 300 g.

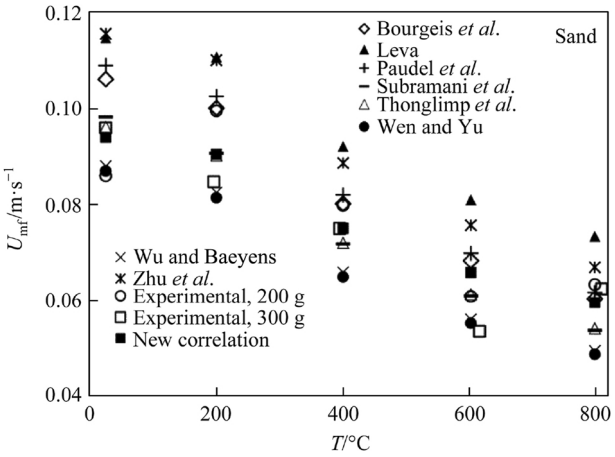


Fig. 13. The variation of the predicted and experimental U_{mf} values with the increasing temperature for silica sand masses of 200 g and 300 g.

$$\Delta P_d = (0.2 - 0.4)\Delta P_{bed} \tag{10}$$

$$\frac{\Delta P_d}{\Delta P_{bed}} \geq 0.14 \tag{11}$$

3.3. Temperature influence on bed pressure drop and minimum fluidization velocity

The relationship between the pressure drop within the bed of the BFBG reactor and the superficial velocity of the fluidizing gas (air velocity) is shown in Fig. 10. The data is presented for temperatures up to 805 °C and two different bed material masses of 200 g and 300 g.

Throughout the fixed-bed phase, there was a consistent linear increase in bed pressure across all temperature variations. The transition from the fixed-bed state to fluidization was smooth in every scenario, attributed to the uniformly packed bed and the narrow size distribution of the silica sand particles. However, upon achieving complete fluidization, the bed pressure began to rise gradually with increasing U_g due to pronounced wall effects caused by strong particle-wall adhesion, and it exceeded the theoretical bed pressure drop value ($\Delta P_{bed} = mg/A$) of 1.72 kPa and 2.58 kPa for Case I and Case II, respectively. This departure from the ideal plateau after complete fluidization is consistent with the hydrodynamics of a narrow-deep bubbling fluidized bed due to the higher wall shear stress and particle–wall interactions. The higher bed aspect ratio resulted in a sharper increase in pressure drop, which is consistent with this observation. Similar trends in pressure drop were observed in studies by Olatunde *et al.* [35] and Srivastava and Sundaresan [36].

Contrarily, Fig. 10 also demonstrates that an increase in temperature led to a reduction in U_{mf} for both bed aspect ratios. This decline was ascribed to the elevated drag coefficient linked with lower Reynolds numbers at higher temperatures [19]. Observations showed that the range between the complete and initial fluidization velocities decreased as the temperature rose. Temperature had an impact on the bed voidage [37], interparticle forces [38], and viscosity of the fluidizing gas, which led to an increase in the bed pressure drop. The increase in the bed voidage was attributed to the intensified interparticle forces in the absence of flow in the bed by Formisani *et al.* [37].

The variations in ΔP_{mf}, U_{mf}, *Ar*, and *Re* with temperature are summarized in Table 4. These parameters are sensitive to temperature alterations, which are impacted by the viscosity and density changes of the fluidizing gas. *Ar* and *Re* values were computed to compare the experimental U_{mf} against theoretical forecasts. Observations revealed that ΔP_{mf} increased by 5% from ambient conditions to the maximum temperature of 805 °C. Conversely, U_{mf}, *Ar*, and Re_{mf} decreased by 27%, 93%, and 90% respectively for 200 g of sand. Similarly, for 300 g of sand, although ΔP_{mf} increased by the same 5% from the minimum to the maximum temperature, U_{mf}, *Ar*, and Re_{mf} decreased by 35%, 93%, and 92% respectively.

3.4. Comparative analysis with existing literature correlations

There have been numerous correlations derived to predict U_{mf} since the earliest applications of fluidized beds. However, very few research studies accounted for the temperature effect. In this study, empirical data acquired under ambient and hot conditions were all evaluated together. In addition, the bed aspect ratio was also considered an important factor that affects the U_{mf} at higher temperatures than ambient. In this section, some correlations found in the literature with our experimental findings were compared. Furthermore, a recently formulated correlation was

utilized to compute the U_{mf} and compare it with the experimental data.

As seen in Fig. 11, *Re* increases with the increase of the *Ar* (see Table 4). The trend line of the *Re* obtained from the experimental data for both 200 g and 300 g shows almost a linear increase with *Ar*. A new correlation (mentioned as A9 in Table 5) shown in Eq. (12) has been derived according to the trend line obtained from the experimental data. The accuracy of the new correlation is represented by the error percentage (Error, %) for each total mass (bed aspect ratio). Error is calculated with Eq. (13) and the experimental data as the nominal value.

$$Re_{mf} = 0.001Ar^{0.9438} \tag{12}$$

$$\text{Error} = \frac{|E - A|}{A} \times 100\% \tag{13}$$

Table 5 summarizes the experimental Re_{exp} at each temperature for the 200 g and 300 g beds and compares these values with predictions from literature correlations (A1–A8) and the newly developed correlation A9. For clarity, the predicted *Re* are presented with two decimal places, whereas the error values were calculated using the original (unrounded) predictions to ensure accuracy. For each correlation, the table reports both the prediction and the error (%) values relative to the experimental Re_{exp}.

The newly derived correlation (A9) could predict the minimum fluidization velocity with average errors of 7.7% and 7.2% for 200 g and 300 g silica sand, respectively. In the pool of correlations analyzed, the one proposed by Thonglimp *et al.* (A5) [29] demonstrated the closest agreement with the experimentally determined *Re*. This correlation exhibited average relative errors of 9% and 7% for Case I and Case II, respectively, showcasing its effectiveness in predicting *Re* across varying conditions. On the other hand, the correlation derived by Leva (A2) [26] had higher relative errors, reaching a maximum of 22% for Case I and 29% for Case II. Noteworthy predictions were also made by Subramani *et al.* (A4) [28], with average relative errors of 9.7% for Case I and 8% for Case II, respectively. Fig. 12 provides a visual representation of the changes in both predictions of *Re* and experimental *Re* with respect to the *Ar*, considering total masses of 200 g (Fig. 12(a)) and 300 g (Fig. 12(b)). Fig. 13 presents the change in the predicted and experimental U_{mf} values with increasing temperature. The error percentages exhibited similarities to those depicted in Table 5, as U_{mf} is dependent on the *Re*.

4. Conclusions

This study investigated the hydrodynamics of a narrow-deep bubbling fluidized bed from ambient temperature up to 805 °C. Two separate experimental setups (a transparent cold flow rig and a bench-scale bubbling fluidizing bed reactor with dimensions similar to the cold flow rig) were utilized to measure the pressure drop variations through the distributor plate and across the bed at two bed aspect ratios (3.33 and 4.83) and various fluidization velocities. The bed material was Geldart Group B silica sand with high sphericity. The main conclusions are summarized as:

(1) The temperature rise resulted in a decrease in the minimum fluidization velocity.
(2) An increase in the bed aspect ratio did not significantly affect U_{mf}, irrespective of the bed temperature. However, the bed aspect ratio affected the bed pressure drop and the corresponding transition from bubbling bed to turbulent bed.
(3) There were significant differences between the non-dimensional *Ar* and *Re* numbers calculated using the data from this study and those derived from established empirical correlations in the literature, which support the need for further investigations.

CRediT Authorship Contribution Statement

Ali Can Sivri: Writing – review & editing, Writing – original draft, Visualization, Validation, Supervision, Methodology, Investigation, Formal analysis, Data curation, Conceptualization. Amoolya Lalsare: Writing – review & editing, Data curation. Xi Gao: Writing – review & editing.

Declaration of Competing Interest

The authors declare that they have no known competing financial interests or personal relationships that could have appeared to influence the work reported in this paper.

Acknowledgements

The research was conducted at WVU's Advanced Combustion Laboratory in Morgantown, WV, and the author gratefully acknowledges WVU's CIGRU, MAE, and CBE departments for their assistance with comprehensive mechanical, electronic, and data-acquisition hardware/software systems, respectively. This work was partially supported by the US Department of Energy's Fossil Energy Advanced Gasification Program and the NETL Research and Innovation Center's Advanced Gasification effort within the Advanced Reaction Systems FWP.

Supplementary Material

Supplementary data to this article can be found online at https://doi.org/10.1016/j.cjche.2025.11.029.

References

[1] A. Lalsare, A. Sivri, R. Egan, R.J. Vukmanovich, C.E. Dumitrescu, J.L. Hu, Biomass–Flare gas synergistic co-processing in the presence of carbon dioxide for the controlled production of syngas (H_2:CO ~ 2–2.5), *Chem. Eng. J.* 385 (2020) 123783.
[2] J. Yu, L.Q. Lu, X. Gao, Y.P. Xu, M. Shahnam, W.A. Rogers, Coupling reduced-order modeling and coarse-grained CFD-DEM to accelerate coal gasifier simulation and optimization, *AIChE J.* 67 (2021) e17030.
[3] A. Lalsare, Y.X. Wang, Q.Y. Li, A. Sivri, R.J. Vukmanovich, C.E. Dumitrescu, J.L. Hu, Hydrogen-rich syngas production through synergistic methane-activated catalytic biomass gasification, *ACS Sustainable Chem. Eng.* 7 (19) (2019) 16060–16071.
[4] A.C. Sivri, A study on the hydrodynamics of a bench-scale top-fed bubbling fluidized bed gasifier using biomass and coal as feedstocks. Ph. D. Thesis, West Virginia Univ., America, 2020.
[5] S. Wang, K. Luo, C.S. Hu, L.Y. Sun, J.R. Fan, Impact of operating parameters on biomass gasification in a fluidized bed reactor: an eulerian-lagrangian approach, *Powder Technol.* 333 (2018) 304–316.
[6] A.C. Sivri, Fluidization behavior of binary mixtures of coal in a top-fed bubbling fluidized bed gasifier, in: Recent Advances for Coal Energy in the 21st Century, IntechOpen, UK, 2024.
[7] Y. Li, Y.X. Yu, C. Zhang, Z.Q. Huang, Q. Zhou, Improved filtered mesoscale interphase heat transfer model, *Particuology* 57 (2021) 176–186.
[8] B. Wang, J.J. Dai, S.J. Li, Y.X. Lin, M. Patrascu, X. Gao, Coupling coarse-grained DEM-CFD and intraparticle model for biomass fast pyrolysis simulation and experiment validation, *AIChE J.* 70 (5) (2024) e18393.
[9] L.Q. Lu, X. Gao, J.F. Dietiker, M. Shahnam, W.A. Rogers, MFiX based multi-scale CFD simulations of biomass fast pyrolysis: a review, *Chem. Eng. Sci.* 248 (2022) 117131.
[10] J. Yu, L.Q. Lu, Y.P. Xu, X. Gao, M. Shahnam, W. Rogers, Coarse-grained CFD-DEM simulation and the design of an industrial-scale coal gasifier, *Ind. Eng. Chem. Res.* 61 (1) (2022) 866–881.

[11] T. Zhou, S.L. Yang, Y.G. Wei, J.H. Hu, H. Wang, Impact of wide particle size distribution on the gasification performance of biomass in a bubbling fluidized bed gasifier, *Renew. Energy* 148 (2020) 534–547.
[12] D. Geldart, Types of gas fluidization, *Powder Technol.* 7 (5) (1973) 285–292.
[13] P. Lettieri, D. Macrì, Effect of process conditions on fluidization, *KONA Powder Part. J.* 33 (2016) 86–108.
[14] R. Grim, Hydrodynamics of fluidized beds under reaction conditions, Master Thesis, Eindhoven University of Technology, Netherlands, 2015.
[15] M.T. Lim, Z. Alimuddin, Bubbling fluidized bed biomass gasification: performance, process findings and energy analysis, *Renew. Energy* 33 (10) (2008) 2339–2343.
[16] X. Wu, K. Li, F.Y. Song, X.F. Zhu, Fluidization behavior of biomass particles and its improvement in a cold visualized fluidized bed, *Bioresources* 12 (2) (2017) 3546–3559.
[17] W.G. Lin, K. Dam-Johansen, F. Frandsen, Agglomeration in bio-fuel fired fluidized bed combustors, *Chem. Eng. J.* 96 (1–3) (2003) 171–185.
[18] S.C. Saxena, A. Mathur, Minimum fluidization velocity at high temperatures, *Ind. Eng. Chem. Res.* 26 (4) (1987) 859–860.
[19] J.S.M. Botterill, Y. Teoman, Y. Teoman, K.R. Yüregir, The effect of temperature on fluidized bed behaviour, *Chem. Eng. Commun.* 15 (1–4) (1982) 227–238.
[20] A. Al-Farraji, H. Taofeeq, Effect of elevated temperature and silica sand particle size on minimum fluidization velocity in an atmospheric bubbling fluidized bed, *Chin. J. Chem. Eng.* 28 (12) (2020) 2985–2992.
[21] A. Anantharaman, R.A. Cocco, J.W. Chew, Evaluation of correlations for minimum fluidization velocity (U_{mf}) in gas-solid fluidization, *Powder Technol.* 323 (2018) 454–485.
[22] J.G. Yates, Effects of temperature and pressure on gas-solid fluidization, *Chem. Eng. Sci.* 51 (2) (1996) 167–205.
[23] B.C. Lippens, J. Mulder, Prediction of the minimum fluidization velocity, *Powder Technol.* 75 (1) (1993) 67–78.
[24] S. Ergun, Fluid flow through packed columns, *Chem. Eng. Prog.* 48 (2) (1952) 89–94.
[25] P. Bourgeois, P. Grenier, The ratio of terminal velocity to minimum fluidising velocity for spherical particles, *Can. J. Chem. Eng.* 46 (5) (1968) 325–328.
[26] M. Leva, Fluid Flow Through Packed and Fluidized Systems, US Government Printing Office, 1951.
[27] B. Paudel, Z.G. Feng, Prediction of minimum fluidization velocity for binary mixtures of biomass and inert particles, *Powder Technol.* 237 (2013) 134–140.
[28] H.J. Subramani, M.B. Mothivel Balaiyya, L.R. Miranda, Minimum fluidization velocity at elevated temperatures for Geldart's group-B powders, *Exp. Therm. Fluid Sci.* 32 (1) (2007) 166–173.
[29] V. Thonglimp, N. Hiquily, C. Laguerie, Vitesse minimale de fluidisation et expansion des couches fluidisées par un gaz, *Powder Technol.* 38 (3) (1984) 233–253.
[30] C.Y. Wen, Y.H. Yu, A generalized method for predicting the minimum fluidization velocity, *AIChE J.* 12 (3) (1966) 610–612.
[31] S.Y. Wu, J. Baeyens, Effect of operating temperature on minimum fluidization velocity, *Powder Technol.* 67 (2) (1991) 217–220.
[32] Z.P. Zhu, Y.J. Na, Q.G. Lu, Effect of pressure on minimum fluidization velocity, *J. Therm. Sci.* 16 (3) (2007) 264–269.
[33] F. Zuiderweg, Design report on fluidization, in: Proceedings of International Symposium on Fluidization, AAH Drinkenburg, 739 (1967).
[34] R. Siegel, Effect of distributor plate-to-bed resistance ratio on onset of fluidized-bed channeling, *AIChE J.* 22 (3) (1976) 590–592.
[35] G. Olatunde, O. Fasina, T. Mcdonald, S. Adhikari, S. Duke, Moisture effect on fluidization behavior of loblolly pine Wood grinds, *Biomass Convers. Biorefinery* 7 (2) (2017) 207–220.
[36] A. Srivastava, S. Sundaresan, Role of wall friction in fluidization and standpipe flow, *Powder Technol.* 124 (1–2) (2002) 45–54.
[37] B. Formisani, R. Girimonte, L. Mancuso, Analysis of the fluidization process of particle beds at high temperature, *Chem. Eng. Sci.* 53 (5) (1998) 951–961.
[38] P. Lettieri, J.G. Yates, D. Newton, The influence of interparticle forces on the fluidization behaviour of some industrial materials at high temperature, *Powder Technol.* 110 (1–2) (2000) 117–127.